Supplementary Material

Piezoelectricity of (K, Na)(Nb, Sb)O$_3$-SrZrO$_3$-(Bi, Ag)ZrO$_3$ piezoceramics and their application to a planar-type actuator

Su-hwan Go[a, †], Jae-min Eum [a, †], Dae-Su Kim[a], Seok-June Chae[a], Sun-Woo Kim[a], Eun-Ji Kim[a], Yeon-Gyeong Chae[a], Jong-Un Woo[b] and Sahn Nahm[a,b,*]

[a]Department of Materials Science and Engineering, Korea University, 145 Anam-ro, Seongbuk-gu, Seoul, 02841, Republic of Korea

[b] Department of Nano Bio Information Technology, KU-KIST Graduate School of Converging Science and Technology, Korea University, 145 Anam-ro, Seongbuk-gu, Seoul, 02841, Republic of Korea

[†]These authors contributed equally to this work.

[*]Corresponding author email address: snahm@korea.ac.kr

1. Experimental procedure for measurement of physical properties of the sample

The crystal structures of the sintered ceramics and thick films were examined using X-ray diffraction analysis (XRD; Shimadzu, XRD-6100, Japan). The peaks at 66.5°, measured by low-speed scanning, were deconvoluted using the Voigt function. For a detailed investigation of the crystal structure of the specimens, XRD patterns were analyzed by the Rietveld method using the FullProf program. The microstructures of the specimens were studied using field-emission scanning electron microscopy (FE-SEM; TESCAN, LYRA3, Czech Republic). Moreover, the domain structures of the specimens were studied using field-emission transmission electron microscopy (FE-TEM; FEI, TECNAI G2 F30, USA) operating at 300 kV. TEM samples were prepared by focused ion beam milling (FIB; Thermo Fisher Scientific, Helios G4 UC, USA). The densities of the sintered specimens were measured using Archimedes' principle.

Silver electrodes were printed on the surfaces of the sintered specimens and fired at 600 °C for 10 min to measure the electrical properties of the specimens. The specimens were poled by applying a DC electric field of 3 kV/mm for 20 min at various temperatures in a silicone oil bath. The dielectric properties were measured using an impedance analyzer (Agilent Technologies, HP 4194A, USA). Variations in the dielectric constant ($\varepsilon^{T}_{33}/\varepsilon_{o}$) and dielectric loss (*tan δ*) were measured with respect to temperature and frequency using an impedance analyzer (Agilent Technologies, HP 4294A, USA). The polarization versus electric field (*P-E*) hysteresis curves were measured using a ferroelectric tester (RT66A, Radiant Co., Ltd.) and a high-voltage amplifier (Trek, 609E-6-L-CE, USA). The piezoelectric charge constant (*d_{33}*) was measured using a *d_{33}* meter (Micro-Epsilon Channel Product, DT-3300, Raleigh, USA).

2. *P-E* hysteresis curves of KNNS-(0.04-x)SZ-xBAZ piezoceramics

Figures S1(a)–(e) exhibit the *P–E* hysteresis curves of the KNNS-(0.04-x)SZ-xBAZ piezoceramics ($0.0 \leq x \leq 0.04$), and the variation in saturated polarization (P_S), remnant polarization (P_r), and coercive field (E_C) with respect to x are displayed in Fig. S1(f). The P_S of the sample with x = 0.0 was approximately 22.7 µC/cm² (Fig. S1(a)); P_S decreased slightly with increasing x, but its variation was not significant, as shown in Fig. S1(f). The P_r slightly increased with the addition of BAZ, and it slightly decreased when x exceeded 0.01, but the variation was insignificant (Fig. S1(f)). The E_C of the specimen with x = 0.0 was approximately 0.56 kV/mm, which varies negligibly with increasing x, as shown in Fig. S1(f). Therefore, the results suggest that all the samples have good ferroelectric properties and they do not change considerably with the addition of BAZ.

Relaxor ceramics generally show slim *P–E* curves with small P_S, P_r, and E_C values.[1-3] Therefore, it was expected that the P_S, P_r, and E_C values of the KNNS-(0.04-x)SZ-xBAZ piezoceramics ($0.0 \leq x \leq 0.04$) would be reduced by an increase in x because of the increase in the relaxor characteristics. However, the KNNS-(0.04-x)SZ-xBAZ piezoceramics ($0.0 \leq x \leq 0.04$) showed similar *P–E* curves (Figs. S1(a)–(f)). In general, piezoceramics with large grains have exhibited large P_r (or P_S) values because the clamping of the domain walls decreased with an increase in the grain size as a result of the decrease in the grain boundaries.[4, 5] The ferroelectric KNNS-0.04SZ piezoceramic (x = 0.0) has a microstructure consisting of small grains (1.0 µm) and large grains (20 µm), as shown in Fig. 2(a). However, the relaxor KNNS-(0.04-x)SZ-xBAZ piezoceramics ($0.01 \leq x \leq 0.04$) have large grains (23–25 µm) (Figs. 2(b)–(d)), indicating that the average grain size of the relaxor piezoceramics ($0.01 \leq x \leq 0.04$) is much larger than that of the normal ferroelectric piezoceramic (x = 0.0). Therefore, the small difference in the P_r (or P_S) values between the normal ferroelectric piezoceramic (KNNS-0.04SZ piezoceramic) and relaxor piezoceramics (KNNS-(0.04-x)SZ-xBAZ piezoceramics with $0.01 \leq x \leq 0.04$) could be explained by the presence of large grains in the relaxor piezoceramics, which increased the P_r (or P_S) values of the relaxor piezoelectric ceramics.

Moreover, the KNNS-0.04SZ-piezoceramic (x = 0.0) has a T-O-R multi-structure, but the proportion of the T structure is very small, and its structure is close to that of the O-R multi-structure (Figs. S4(a) and (b)). The proportion of the T structure increased with x, and the KNNS-(0.04-x)SZ-xBAZ piezoceramic with x = 0.04 had a T-R multi-structure with a large proportion of T structure (Figs. S4(c)-(f) and Figs. S5(a) and (b)). In general, a piezoceramic

with the T structure has a large E_C value,[6, 7] indicating that the E_C value is expected to increase with x as a result of the increase in the proportion of the T structure. Therefore, the large E_C values of the relaxor KNNS-(0.04-x)SZ-xBAZ piezoceramics (0.01 ≤ x ≤ 0.04) could be explained by the increased proportion of the T structure. The above results suggest that the typical ferroelectric P–E curves with large P_S, P_r, and E_C values for the relaxor KNNS-(0.04-x)SZ-xBAZ piezoceramics (0.01 ≤ x ≤ 0.04) could be explained by their large grains and the increased proportion of the tetragonal structure. However, further studies are required to clearly identify why the relaxor KNNS-(0.04-x)SZ-xBAZ piezoceramics (0.01 ≤ x ≤ 0.04) showed typical ferroelectric P–E curves with large P_S, P_r, and E_C values.
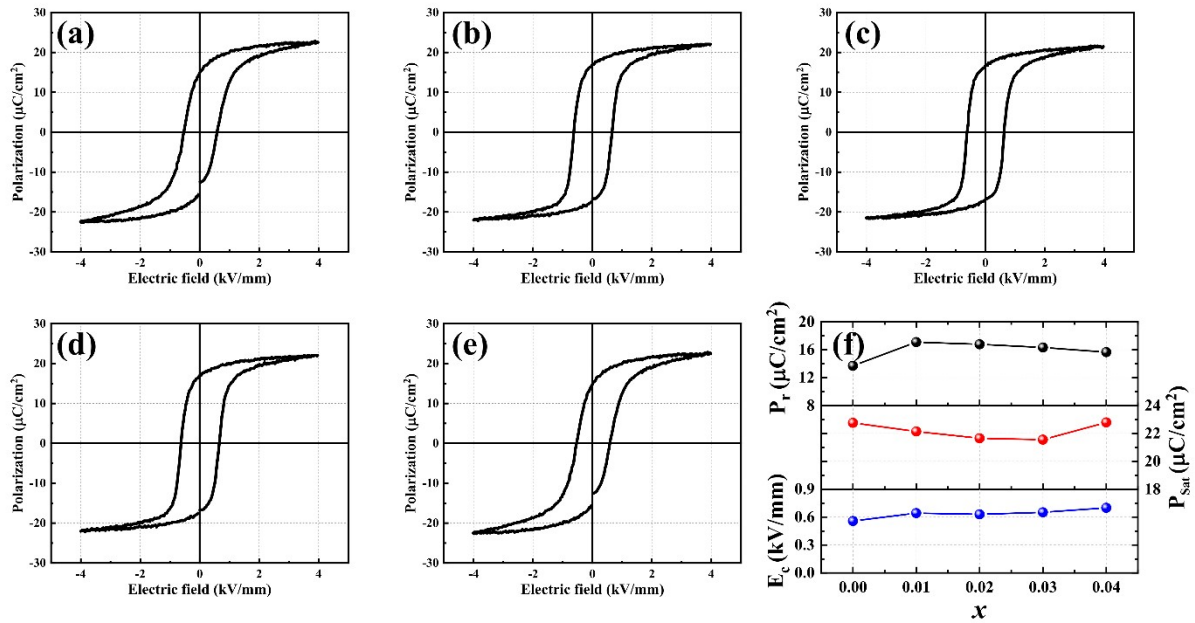

Figure S1. P–E hysteresis curves of the KNNS-(0.04-x)SZ-xBAZ piezoceramics with (a) x = 0.0, (b) x = 0.01, (c) x = 0.02, (d) x = 0.03, and (e) x = 0.04. (f) P_S, P_r, and E_C values of the KNNS-(0.04-x)SZ-xBAZ piezoceramics with 0.0 ≤ x ≤ 0.04.

3. SEM images of the fractured surface of KNNS-(0.04-x)SZ-xBAZ piezoceramics

Figures S2(a)–(e) show the SEM images of the fractured surface of the KNNS-(0.04-x)SZ-xBAZ piezoceramics with $0.0 \leq x \leq 0.04$. All samples exhibited dense microstructures. The piezoceramic with x = 0.0 has a microstructure consisting of large and small grains, as shown in Fig. S2(a)), and the inset shows an enlarged SEM image of the small grains. The average grain sizes of the large and small grains are approximately 20 μm and 1 μm, respectively, (Fig. S2(a)). When BAZ was added, the small grains disappeared (Figs. S2(b)-(e)). The size of the large grains did not change with the increase in BAZ content, and the piezoceramics with 0.01 $\leq x \leq 0.04$ exhibited an identical grain size of approximately 23–25 μm. Similar results were observed for the thermally etched samples, as shown in Figs. 2(a)–(e).

The d_{33} values and relative densities of the KNN-based piezoceramics reported in the literature are listed in Table S1. A few KNN-based piezoceramics had high relative densities ($\geq 97\%$ of the theoretical density), but their d_{33} values were not high, ranging between 350 and 425 pC/N, implying that the crystal structure and domain structure should also be considered to enhance the d_{33} values of KNN-based piezoceramics. Most of the KNN-based piezoceramics had relative densities that were 95–96% of the theoretical density, and some of them exhibited large d_{33} values (≥ 500 pC/N). In addition, the KNN-based piezoceramics with low relative densities (<95 % of the theoretical density) exhibited small d_{33} values, indicating that the density is also important to improve the d_{33} values of KNN-based piezoceramics. Therefore, it is suggested that KNN-based piezoceramics, which have relative densities in the range of 95–96% of the theoretical density, can have large d_{33} values, but their d_{33} values could be further improved by enhancing their densities.
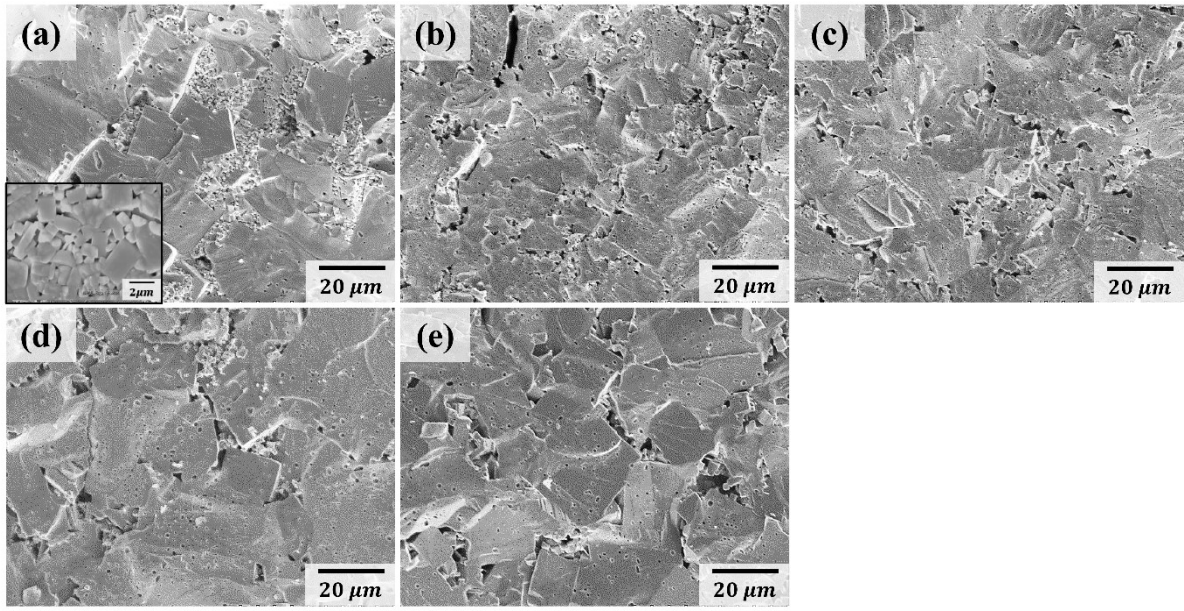
Figure S2. SEM images of the KNNS-(0.04-x)SZ-xBAZ ceramics with $0.0 \leq x \leq 0.04$ sintered at 1090 °C for 3 h: (a) x = 0.0, (b) x = 0.01, (c) x = 0.02, (d) x = 0.03, and (e) x = 0.04

Table S1. The relative densities and d_{33} values of the KNN-based piezoceramics reported in the literature.

Composition	Relative density (%)	d_{33} (pC/N)	ref.
KNN-LTS	98.5	424	8
NKNS-ST	97	358	9
KNNS-CZ-BNH	96.7	450	10
KNNTS-BSNZ	96	510	4
NKNS-CT	96	338	11
LNKNS-CSZ	95	560	12
CLNKNS-CZ	95	502	13
LNKNS-SZ	95	431	14
KNNS-BLAZH-Fe	94-95	343	15
NKNS-SZ	94	325	16
KNNS-BCZ	90	303	17
NKNS-SZ-BAZ	95	650	This work

4. XRD patterns of KNNS-(0.04-x)SZ-xBAZ piezoceramics

Figures S3(a)–(e) show the XRD patterns of the KNNS-(0.04-x)SZ-xBAZ piezoceramics with $0.0 \leq x \leq 0.04$ densified at 1090 °C for 3 h. All the samples have a homogeneous perovskite structure, without secondary phases. Variations in peak position and intensity were not observed with an increase in BAZ content. These results suggest that the addition of BAZ did not change the crystal structure of the samples. However, it is difficult to identify the detailed crystal structures using these normal XRD patterns.
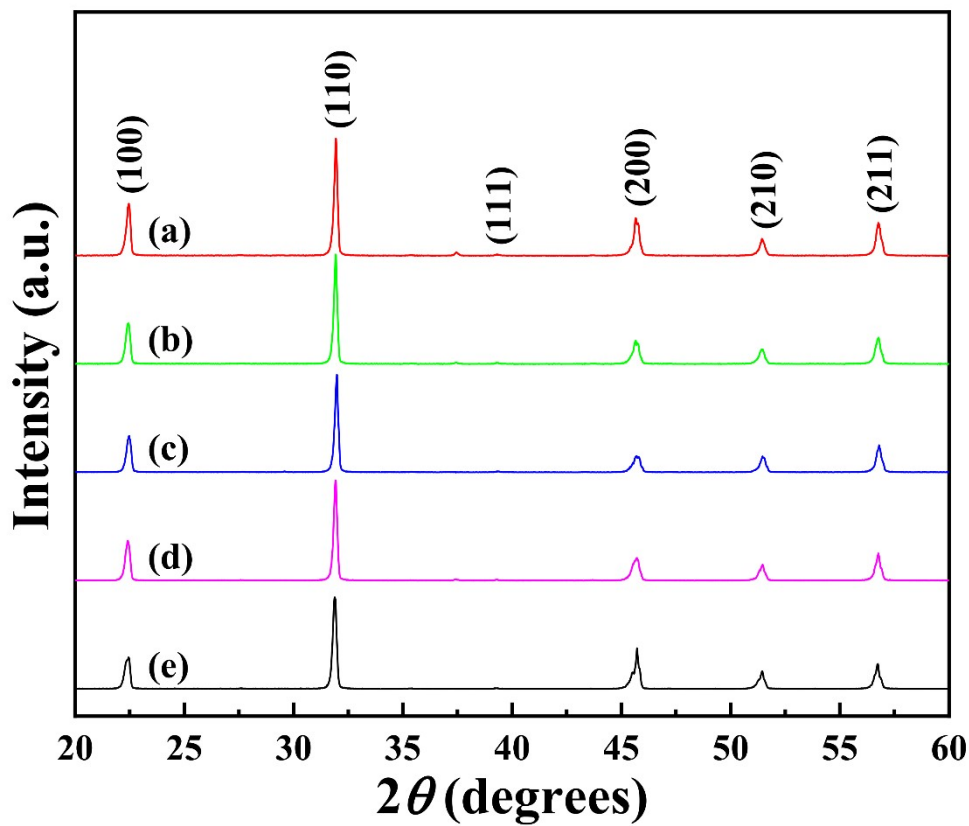

Figure S3. XRD patterns of the KNNS-(0.04-x)SZ-xBAZ piezoceramics sintered at 1090 °C for 3 h: (a) x = 0.0, (b) x = 0.01, (c) x = 0.02, (d) x = 0.03, and (e) x = 0.04.

5. Rietveld refinement XRD profiles of the KNNS-(0.04-x)SZ-xBAZ ceramics

Figures S4(a) and (b) show the Rietveld refinement XRD profile of the KNNS-SZ piezoceramics (x = 0.0) using the O-R multi-structure and T-O-R multi-structure, respectively. The atomic coordinates, site occupancies, lattice parameters, and R-values of these models are listed in Table S1. The R-values of the T-O-R multi-structure were smaller than those of the O-R multi-structure. Therefore, this sample was considered to have a T-O-R multi-structure. The T-O-R multi-structure of this sample consists of 25.2% $R3m$ rhombohedral, 66.2% $Amm2$ orthorhombic, and 8.6% $P4mm$ tetragonal structures, indicating that the proportion of orthorhombic structure is much larger than those of the rhombohedral and tetragonal structures.

Rietveld analysis was also conducted on the XRD pattern of the piezoceramic with x= 0.01, as shown in Figs. S4(c) and (d). The O-R and T-O-R multi-structures were used for Rietveld analysis, and the atomic coordinates, site occupancies, lattice parameters, and R-values of this model are listed in Table S2. The R-values of the T-O-R multi-structure were smaller than those of the O-R multi-structure. Therefore, this specimen was considered to have a T-O-R multi-structure. The T-O-R multi-structure of this sample consists of 25.6% $R3m$ rhombohedral, 58.1% $Amm2$ orthorhombic, and 16.3% $P4mm$ tetragonal structures, indicating that the proportion of orthorhombic structure is also much larger than those of the rhombohedral and tetragonal structures.

Figures S4(e) and (f) show the Rietveld refinement XRD profiles of the KNNS-0.02SZ-0.02BAZ piezoceramic (x = 0.02) and the O-R and T-O-R multi-structures were also used for the Rietveld analysis. Table S3 lists the atomic coordinates, site occupancies, lattice parameters, and R-values of these models. This specimen is considered to have a T-O-R multi-structure because the R-values of this structure are smaller than those of the O-R multi-structure. Moreover, the T-O-R multi-structure of this specimen consists of 24.8% $R3m$ rhombohedral, 53.8% $Amm2$ orthorhombic, and 21.4% $P4mm$ tetragonal structures. Therefore, the proportion of the orthorhombic structure is still larger than that of the rhombohedral and tetragonal structures.
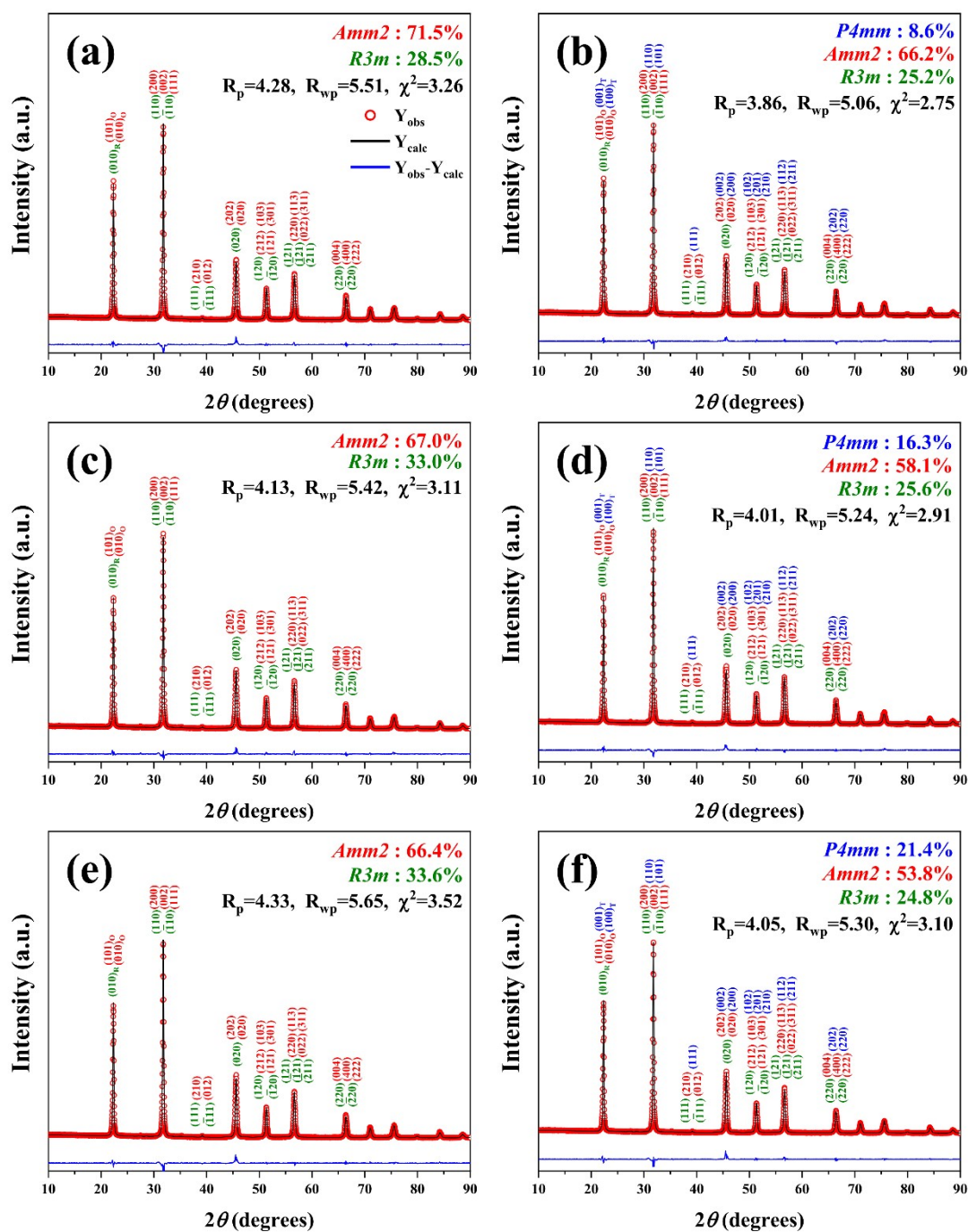
Figure S4. Rietveld refinement XRD profiles of the KNNS-(0.04-x)SZ-xBAZ ceramics with; (a) x = 0.0 (O-R multi-structure), (b) x = 0.0 (T-O-R multi-structure), (c) x = 0.01 (O-R multi-structure), (d) x = 0.01 (T-O-R multi-structure), (e) x = 0.02 (O-R multi-structure), and (f) x = 0.02 (T-O-R multi-structure).

Table S2. Atomic coordinates, site occupancies, lattice parameters, and *R*-values of the KNNS-0.04SZ ceramic at RT for O-R and T-O-R multi-structures

Phase	Structural model (SG)	Site label	x	y	z	Site occupancy	Lattice parameter (Å)	R factor
O-R multi-structure	Orthorhombic (Amm2) (71%) + Rhombohedral (R3m, H) (29%)	K/Na/Ca	0(-)	0(-)	0(-)	0.114(-)/0.123(-)/0.010(-)	a=3.9840(1) b=5.6183(1) c=5.6194(1) $\alpha=\beta=\gamma=90°$	$R_p/R_{wp}/R_{exp}$ R_b/R_f 4.28 / 5.51 / 3.05 4.11 / 1.85
		Nb/Sb/Zr	0.5(-)	0(-)	0.5284(19)	0.224(-)/0.016(-)/0.010(-)		
		O1	0(-)	0(-)	0.5053(89)	0.250(-)		
		O2	0.5(-)	0.2739(-)	0.3074(50)	0.500(-)		
		K/Na/Ca	0(-)	0(-)	0.5050(37)	0.076(-)/0.082(-)/0.007(-)	a=b=5.6416(32) c=6.8746(77) $\alpha=\beta=90°$ $\gamma=120°$	$R_p/R_{wp}/R_{exp}$ R_b/R_f 4.28 / 5.51 / 3.05 3.14 / 1.49
		Nb/Sb/Zr	0(-)	0(-)	0(-)	0.150(-)/0.010(-)/0.007(-)		
		O1	0.5109(-)	-0.5109(-)	0.5184(38)	0.500(-)		
T-O-R multi-structure	Tetragonal (P4mm) (9%) + Orthorhombic (Amm2) (66%) + Rhombohedral (R3m, H) (25%)	K/Na/Ca	0(-)	0(-)	0.0799(403)	0.057(-)/0.062(-)/0.005(-)	a=b=3.9651(7) c=4.0030(11) $\alpha=\beta=\gamma=90°$	$R_p/R_{wp}/R_{exp}$ R_b/R_f 3.86 / 5.06 / 3.05 3.61 / 2.46
		Nb/Sb/Zr	0.5(-)	0.5(-)	0.5(-)	0.112(-)/0.008(-)/0.005(-)		
		O1	0.5(-)	0.5(-)	0.0208(-)	0.125(-)		
		O2	0.5(-)	0(-)	0.5476(168)	0.250(-)		
		K/Na/Ca	0(-)	0(-)	0(-)	0.114(-)/0.123(-)/0.007(-)	a=3.9697(2) b=5.6253(2) c=5.6339(2) $\alpha=\beta=\gamma=90°$	$R_p/R_{wp}/R_{exp}$ R_b/R_f 3.86 / 5.06 / 3.05 3.53 / 2.40
		Nb/Sb/Zr	0.5(-)	0(-)	0.5135(31)	0.224(-)/0.016(-)/0.010(-)		
		O1	0(-)	0(-)	0.4730(44)	0.250(-)		
		O2	0.5(-)	0.1816(18)	0.2429(41)	0.500(-)		
		K/Na/Ca	0(-)	0(-)	0.4885(39)	0.076(-)/0.082(-)/0.007(-)	a=b=5.6229(19) c=6.9163(42) $\alpha=\beta=90°$ $\gamma=120°$	$R_p/R_{wp}/R_{exp}$ R_b/R_f 3.86 / 5.06 / 3.05 2.55 / 1.81
		Nb/Sb/Zr	0(-)	0(-)	0(-)	0.150(-)/0.010(-)/0.007(-)		
		O	0.5109(-)	-0.5109(-)	0.4869(81)	0.500(-)		

Table S3. Atomic coordinates, site occupancies, lattice parameters, and *R*-values of the KNNS-0.03SZ-0.01BAZ ceramic at RT for O-R and T-

O-R multi-structures

Phase	Structural model (SG)	Site label	x	y	z	Site occupancy	Lattice parameter (Å)	R factor
O-R multi-structure	Orthorhombic (Amm2) (67%) + Rhombohedral (R3m, H) (33%)	K/Na/Ca/Bi/Ag	0(-)	0(-)	0(-)	0.114(-)/0.123(-)/0.007(-)/0.001(-)/(0.001(-)	a=3.9856(1) b=5.6197(1) c=5.6200(1) $\alpha = \beta = \gamma = 90°$	$R_p/R_{wp}/R_{exp}$ R_b/R_f 4.13 / 5.42 / 3.07 3.48 / 2.05
		Nb/Sb/Zr	0.5(-)	0(-)	0.5248(33)	0.224(-)/0.016(-)/0.010(-)		
		O1	0(-)	0(-)	0.6060(59)	0.250(-)		
		O2	0.5(-)	0.2494(40)	0.2756(-)	0.500(-)		
		K/Na/Ca/Bi/Ag	0(-)	0(-)	0.4683(31)	0.076(-)/0.082(-)/0.005(-)/0.001(-)/0.001(-)	a=b=5.6360(16) c=6.8874(41) $\alpha = \beta = 90°$ $\gamma = 120°$	$R_p/R_{wp}/R_{exp}$ R_b/R_f 4.13 / 5.42 / 3.07 2.97 / 1.36
		Nb/Sb/Zr	0(-)	0(-)	0(-)	0.150(-)/0.010(-)/0.007(-)		
		O1	0.5109(-)	-0.5109(-)	0.4849(35)	0.500(-)		
T-O-R multi-structure	Tetragonal (P4mm) (16%) + Orthorhombic (Amm2) (58%) + Rhombohedral (R3m, H) (26%)	K/Na/Ca/Bi/Ag	0(-)	0(-)	0.0341(85)	0.057(-)/0.062(-)/0.004(-)/0.001(-)/0.001(-)	a=b=3.9709(6) c=3.9989(5) $\alpha = \beta = \gamma = 90°$	$R_p/R_{wp}/R_{exp}$ R_b/R_f 4.01 / 5.24 / 3.07 4.44 / 2.95
		Nb/Sb/Zr	0.5(-)	0.5(-)	0.5(-)	0.112(-)/0.008(-)/0.005(-)		
		O1	0.5(-)	0.5(-)	0.0208(-)	0.125(-)		
		O2	0.5(-)	0(-)	0.4711(179)	0.250(-)		
		K/Na/Ca	0(-)	0(-)	0(-)	0.114(-)/0.123(-)/0.007(-)	a=3.9719(2) b=5.6289(2) c=5.6376(2) $\alpha = \beta = \gamma = 90°$	$R_p/R_{wp}/R_{exp}$ R_b/R_f 4.01 / 5.24 / 3.07 3.86 / 2.13
		Nb/Sb/Zr	0.5(-)	0(-)	0.4860(41)	0.224(-)/0.016(-)/0.010(-)		
		O1	0(-)	0(-)	0.4588(85)	0.250(-)		
		O2	0.5(-)	0.2127(45)	0.1879(72)	0.500(-)		
		K/Na/Ca/Bi/Ag	0(-)	0(-)	0.4670(51)	0.076(-)/0.082(-)/0.005(-)/0.001(-)/0.001(-)	a=b=5.6332(15) c=6.8866(37) $\alpha = \beta = 90°$ $\gamma = 120°$	$R_p/R_{wp}/R_{exp}$ R_b/R_f 4.01 / 5.24 / 3.07 3.91 / 2.45
		Nb/Sb/Zr	0(-)	0(-)	0(-)	0.150(-)/0.010(-)/0.007(-)		
		O	0.5109	-0.5109(-)	0.4782(51)	0.500(-)		

Table S4. Atomic coordinates, site occupancies, lattice parameters, and *R*-values of the KNNS-0.02SZ-0.02BAZ ceramic at RT for O-R and T-O-R multi-structures

Phase	Structural model (SG)	Site label	x	y	z	Site occupancy	Lattice parameter (Å)	R factor
O-R multi-structure	Orthorhombic (Amm2) (66%) + Rhombohedral (R3m, H) (34%)	K/Na/Ca /Bi/Ag	0(-)	0(-)	0(-)	0.114(-)/0.123(-)/0.005(-)/0.002(-)/(0.002(-)	a=3.9881(2) b=5.6171(2) c=5.6241(2) $\alpha = \beta = \gamma = 90°$	$R_p/R_{wp}/R_{exp}$ R_b/R_f 4.33 / 5.65 / 3.01 4.62 / 2.36
		Nb/Sb/Zr	0.5(-)	0(-)	0.4999(37)	0.224(-)/0.016(-)/0.010(-)		
		O1	0(-)	0(-)	0.5457(116)	0.250(-)		
		O2	0.5(-)	0.2844(84)	0.2497(91)	0.500(-)		
		K/Na/Ca /Bi/Ag	0(-)	0(-)	0.4568(26)	0.076(-)/0.082(-)/0.003(-)/0.002(-)/0.002(-)	a=b=5.6384(26) c=6.8766(62) $\alpha = \beta = 90°$ $\gamma = 120°$	$R_p/R_{wp}/R_{exp}$ R_b/R_f 4.33 / 5.65 / 3.01 3.95 / 2.48
		Nb/Sb/Zr	0(-)	0(-)	0(-)	0.150(-)/0.010(-)/0.007(-)		
		O1	0.5109(-)	-0.5109(-)	0.4822(66)	0.500(-)		
T-O-R multi-structure	Tetragonal (P4mm) (21%) + Orthorhombic (Amm2) (54%) + Rhombohedral (R3m, H) (25%)	K/Na/Ca /Bi/Ag	0(-)	0(-)	0.2454(600)	0.057(-)/0.062(-)/0.002(-)/0.001(-)/0.001(-)	a=b=3.9675(4) c=3.9920(4) $\alpha = \beta = \gamma = 90°$	$R_p/R_{wp}/R_{exp}$ R_b/R_f 4.05 / 5.30 / 3.01 3.62 / 1.93
		Nb/Sb/Zr	0.5(-)	0.5(-)	0.5(-)	0.112(-)/0.008(-)/0.005(-)		
		O1	0.5(-)	0.5(-)	0.0243(-)	0.125(-)		
		O2	0.5(-)	0(-)	0.3689(421)	0.250(-)		
		K/Na/Ca	0(-)	0(-)	0(-)	0.114(-)/0.123(-)/0.007(-)	a=3.9697(2) b=5.6253(2) c=5.6339(2) $\alpha = \beta = \gamma = 90°$	$R_p/R_{wp}/R_{exp}$ R_b/R_f 3.86 / 5.06 / 3.05 3.53 / 2.40
		Nb/Sb/Zr	0.5(-)	0(-)	0.5135(31)	0.224(-)/0.016(-)/0.010(-)		
		O1	0(-)	0(-)	0.4730(44)	0.250(-)		
		O2	0.5(-)	0.1816(18)	0.2429(41)	0.500(-)		
		K/Na/Ca /Bi/Ag	0(-)	0(-)	0.4531(31)	0.076(-)/0.082(-)/0.003(-)/0.002(-)/0.002(-)	a=b=5.6442(30) c=6.8831(64) $\alpha = \beta = 90°$ $\gamma = 120°$	$R_p/R_{wp}/R_{exp}$ R_b/R_f 4.05 / 5.30 / 3.01 2.58 / 1.60
		Nb/Sb/Zr	0(-)	0(-)	0(-)	0.150(-)/0.010(-)/0.007(-)		
		O	0.5109(-)	-0.5109(-)	0.5380(67)	0.500(-)		

6. Rietveld refinement XRD profiles of the KNNS-0.04 BAZ ceramics

Figures S5(a) and (b) display the Rietveld refinement XRD profiles of the KNNS-0.04BAZ piezoceramic (x = 0.04) using the T-O-R multi-structure and the R-T multi-structure, respectively. The atomic coordinates, site occupancies, lattice parameters, and R-values of these models are listed in Table S4. The R-values of the R-T multi-structure are smaller than those of the T-O-R multi-structure. Hence, this sample is expected to have an R-T multi-structure. This R-T multi-structure consists of 29% $R3m$ rhombohedral and 71% $Pm3m$ tetragonal structures. Therefore, the proportion of the tetragonal structure is larger than that of the rhombohedral structure.
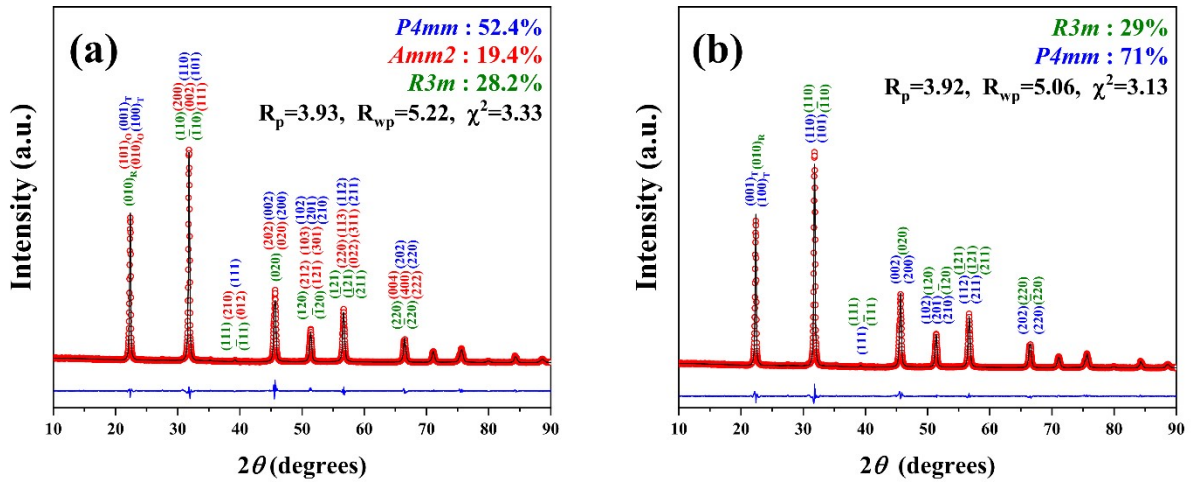

Figure S5. Rietveld refinement XRD profiles of the KNNS-0.04BAZ piezoceramic (x=0.04) using; (a) T-O-R multi-structure and (b) x = R-T multi-structure.

Table S5. Atomic coordinates, site occupancies, lattice parameters, and *R*-values of the KNNS-0.04BAZ ceramic at RT for T-O-R and R-T multi-structures

Phase	Structural model (SG)	Site label	x	y	z	Site occupancy	Lattice parameter (Å)	R factor
T-O-R multi-structure	Tetragonal (P4mm) (53%) + Orthorhombic (Amm2) (19%) + Rhombohedral (R3m, H) (28%)	K/Na /Bi/Ag	0(-)	0(-)	0.0381(44)	0.057(-)/0.062(-) /0.002(-)/0.002(-)	a=b=3.9752(1) c=3.9792(1) $\alpha = \beta = \gamma = 90°$	$R_p/R_{wp}/R_{exp}$ R_b/R_f 3.93 / 5.22 / 2.86 2.77 / 1.68
		Nb/Sb/Zr	0.5(-)	0.5(-)	0.5(-)	0.112(-)/0.008(-)/0.005(-)		
		O1	0.5(-)	0.5(-)	-0.0381(206)	0.125(-)		
		O2	0.5(-)	0(-)	0.4449(36)	0.250(-)		
		K/Na /Bi/Ag	0(-)	0(-)	0(-)	0.114(-)/0.123(-) /0.005(-)/0.005(-)	a=3.9953(3) b=5.5973(4) c=5.6179(3) $\alpha = \beta = \gamma = 90°$	$R_p/R_{wp}/R_{exp}$ R_b/R_f 3.93 / 5.22 / 2.86 3.55 / 2.74
		Nb/Sb/Zr	0.5(-)	0(-)	0.4926(36)	0.224(-)/0.016(-)/0.010(-)		
		O1	0(-)	0(-)	0.4105(115)	0.250(-)		
		O2	0.5(-)	0.2739(-)	0.2585(-)	0.500(-)		
		K/Na /Bi/Ag	0(-)	0(-)	0.4473(50)	0.076(-)/0.082(-) /0.003(-)/0.003(-)	a=b=5.6381(33) c=6.8800(82) $\alpha = \beta = 90°$ $\gamma = 120°$	$R_p/R_{wp}/R_{exp}$ R_b/R_f 3.93 / 5.22 / 2.86 2.23 / 1.68
		Nb/Sb/Zr	0(-)	0(-)	0(-)	0.150(-)/0.010(-)/0.007(-)		
		O	0.5109(-)	-0.5109(-)	0.4841(-)	0.500(-)		
R-T multi-structure	Rhombohedral (R3m, H) (29%) + Tetragonal (P4mm) (71%)	K/Na /Bi/Ag	0(-)	0(-)	0.5173(53)	0.076(-)/0.082(-) /0.003(-)/0.003(-)	a=b=5.6381(12) c=6.8867(17) $\alpha = \beta = 90°$ $\gamma = 120°$	$R_p/R_{wp}/R_{exp}$ R_b/R_f 3.92 / 5.06 / 2.86 2.44 / 1.35
		Nb/Sb/Zr	0(-)	0(-)	0(-)	0.150(-)/0.010(-)/0.007(-)		
		O1	0.4951(-)	-0.4951(-)	0.4629(38)	0.500(-)		
		K/Na /Bi/Ag	0(-)	0(-)	0.0440(48)	0.057(-)/0.062(-) /0.002(-)/0.002(-)	a=b=3.9701(2) c=3.9881(2) $\alpha = \beta = \gamma = 90°$	$R_p/R_{wp}/R_{exp}$ R_b/R_f 3.92 / 5.06 / 2.86 2.10 / 1.54
		Nb/Sb/Zr	0.5(-)	0.5(-)	0.5(-)	0.112(-)/0.008(-)/0.005(-)		
		O1	0.5(-)	0.5(-)	0.0588(74)	0.125(-)		
		O2	0.5(-)	0(-)	0.4703(62)	0.250(-)		

7. $\varepsilon^T_{33}/\varepsilon_0$ versus temperature curves measured at various frequencies for the KNNS-(0.04-x)SZ-xBAZ ceramics

Figure S6(a) shows the $\varepsilon^T_{33}/\varepsilon_0$ versus temperature curves measured at various frequencies for the specimen with x = 0.01, near a $T_{\text{T-O-R}}$ peak. The $\varepsilon^T_{33}/\varepsilon_0$ value decreased with increasing frequency. Moreover, the $T_{\text{T-O-R}}$ increased with an increase in the frequency, and ΔT was approximately 4.5 °C. Therefore, the specimen with x = 0.01 shows a relaxor characteristic near the $T_{\text{T-O-R}}$ that corresponds to the ferroelectric-to-ferroelectric phase transition temperature. Similar results were observed for the specimen with x = 0.02, and ΔT slightly increased to 5.7 °C, as displayed in Fig. S6(b). Hence, the specimen with x = 0.02 also shows relaxor characteristics near the $T_{\text{T-O}}$. Figure S6(c) shows the $\varepsilon^T_{33}/\varepsilon_0$ versus temperature curves measured at various frequencies for the specimen with x = 0.04. They were measured near the $T_{\text{R-T}}$ peak, which is also a ferroelectric-to-ferroelectric phase transition temperature. The $T_{\text{R-T}}$ peak increased with an increase in frequency, and the ΔT was approximately 14 °C. Therefore, it can be concluded that the specimen with x = 0.04 also shows the relaxor characteristic near the $T_{\text{R-T}}$.

The above results show that ΔT increased with an increase in x, indicating that the addition of BAZ increased the relaxor properties of the samples. Moreover, relaxor properties, which are found in the samples with $0.01 \leq x \leq 0.04$, are observed at the ferroelectric-to-ferroelectric transition temperatures, such as $T_{\text{T-O-R}}$ and $T_{\text{R-T}}$. Therefore, they are different from the traditional relaxor properties that were found near T_C, that is, the ferroelectric-to-paraelectric phase transition temperature.
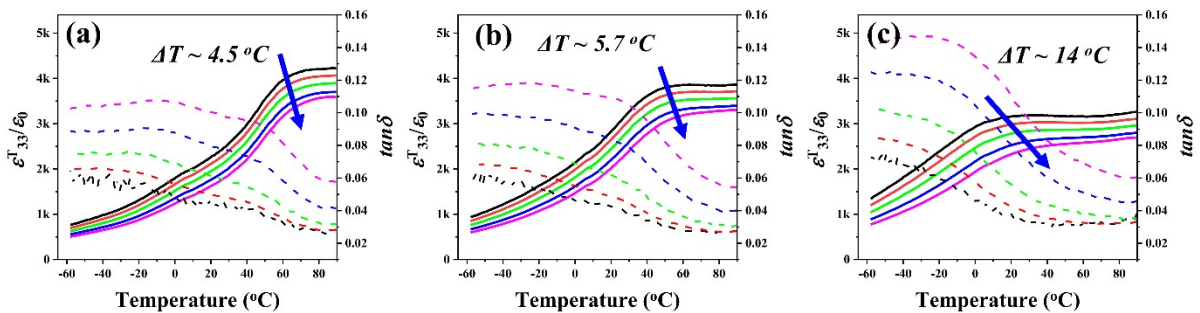

Figure S6. $\varepsilon^T_{33}/\varepsilon_0$ versus temperature curves measured at various frequencies for the KNNS-(0.04-x)SZ-xBAZ ceramics with (a) x = 0.01, (b) x = 0.02, and (c) x = 0.04.

8 . SEM images of the thermally etched KNNS-0.01SZ-0.03BAZ thick films

Figure S7(a) shows an SEM image of the thermally etched surface of the KNNS-0.01SZ-0.03BAZ thick film sintered at 1080 °C for 6 h. Two types of grains were developed in this thick film: large grains and small grains, with average grain sizes of 25 μm and 0.5 μm, respectively. The inset shows an enlarged SEM image of the small-sized grains. The relative density of this thick film was low, at 89% of the theoretical density (Fig. 7(c)). However, when the sintering temperature increased, small grains disappeared, and large grains with an average grain size of approximately 25 μm appeared only in the KNNS-0.01SZ-0.03BAZ thick films, as shown in Figs. S7(b) and (c). The microstructures of these thick films are similar to those of the KNNS-0.01SZ-0.03BAZ piezoceramic sintered at 1090 °C. Moreover, these thick films showed high relative densities ($\geq$ 93% of the theoretical density), as shown in Fig. 7(c). Therefore, it is possible that the presence of the small grains can be explained by the insufficient sintering of the thick film, suggesting that the KNNS-0.01SZ-0.03BAZ thick films should be sintered at temperatures higher than 1080 °C.

The d_{33} values of the KNN-based single crystals and textured KNN-based thick films are listed in Table S6. The d_{33} values of some of the KNN-based singles were larger than those of the KNNS-0.01SZ-0.03BAZ thick film developed in this study. However, most of the KNN-based single crystals showed smaller d_{33} values compared with the d_{33} value of the KNNS-0.01SZ-0.03BAZ tshick film developed in this study. Moreover, only one textured KNN-thick film exhibited a larger d_{33} value (700 pC/N) than that (630 pC/N) of the KNNS-0.01SZ-0.03BAZ thick film developed in this study. Therefore, it can be concluded that the KNNS-0.01SZ-0.03BAZ thick film developed in this study has a high d_{33} value compared to most KNN-based single crystals and KNN-based textured thick films.
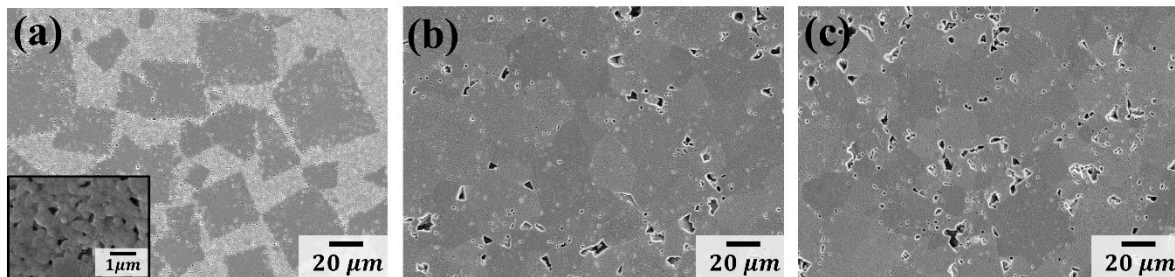

Figure S7. SEM images of the KNNS-0.01SZ-0.03BAZ thick films sintered at various temperatures; (a) 1080°C, (b) 1100°C and (c) 1110°C.

Table S6. The d_{33} values of the KNN-based single crystals and the textured KNN-based thick films reported in the literature.

Composition	Type	d_{33} (pC/N)	ref.
KNN-LB-MnO$_2$	Single crystal	1050	18
KNLNTS	Single crystal	732	19
KNLN	Single crystal	689	20
KNLNT-MnO$_2$	Single crystal	545	21
KNN-LB-CZ	Single crystal	488	22
KNTN	Single crystal	416	23
KNN-MnO2	Single crystal	261	24
KNN-LT	Single crystal	255	25
KNN25/75	Single crystal	145	26
KNNS-CZ-BKH	Textured thick film	700	27
NKNS-SZ	Textured thick film	620	28
KNLNST-CZ	Textured thick film	391	29
KNLNS-CZ	Textured thick film	310	30
NKNS-SZ-BAZ	Thick film	630	This work

9. Simulation of actuating properties of planar-type KNNS-0.01SZ-0.03BAZ actuator

The actuating characteristics of the planar-type KNNS-0.01SZ-0.03BAZ actuator were simulated using the COMSOL program, and the parameters used for the measurement of the actuating properties of this actuator were also employed in the simulation. Figure S8(a) shows the variation in the acceleration with respect to the frequency. The maximum acceleration was observed at a resonance frequency of 620 Hz and it increased with an increase in the applied electric field; the largest acceleration of 330 G was obtained at an electric field of 120 V/mm (36 V). A similar resonance frequency of 610 Hz was obtained from the measurement, as shown in Fig. 8(c), and the calculated maximum accelerations at various applied electric fields are displayed as red circles in the inset of Fig. 8(c). The calculated accelerations were similar to the measured accelerations.

Figure S8(b) shows the variation in the simulated displacement of this actuator with respect to the frequency at various applied electric fields. The maximum displacement was also obtained at 620 Hz and it increased with an increase in the electric field, as indicated by the red circles in the inset of Fig. 8(d). When an electric field of 120 V/mm (36 V) was used for the simulation, the largest displacement of 213 μm was obtained, which is similar to the largest measured displacement (231 μm). The above results clearly show that the simulated results are in good agreement with the measured results.

Figure S8. Variations of (a) the acceleration and (b) displacement with respect to the frequency calculated at various electric fields for the KNNS-0.01SZ-0.03BAZ planar-type actuator.

References

1.   J. Zhang, Z. Liu, T. Zhang, Y. Liu and Y. Lyu, *Journal of Materials Science: Materials in Electronics*, 2021, 1-11.

2.   Y. Guo, K.-i. Kakimoto and H. Ohsato, *Journal of Physics and Chemistry of Solids*, 2004, **65**, 1831-1835.

3.   F. Li, S. Zhang, D. Damjanovic, L. Q. Chen and T. R. Shrout, *Advanced Functional Materials*, 2018, **28**, 1801504.

4.   K. Chen, J. Ma, C. Shi, W. Wu and B. Wu, *Journal of Alloys and Compounds*, 2021, **852**, 156865.

5.   W. Yang, P. Li, S. Wu, F. Li, B. Shen and J. Zhai, *Advanced Electronic Materials*, 2019, **5**, 1900570.

6.   Y. Huan, X. Wang, J. Koruza, K. Wang, K. G. Webber, Y. Hao and L. Li, *Scientific reports*, 2016, **6**, 1-12.

7.   K.-i. Kakimoto, L. T.-K. Nguyen, Y. Hayakawa, Y. Shinkai and I. Kagomiya, *Journal of the Korean Physical Society*, 2011, **59**, 2452-2456.

8.   Y. Huan, X. Wang, Z. Shen, J. Kim, H. Zhou and L. Li, *Journal of the American Ceramic Society*, 2014, **97**, 700-703.

9.   D. H. Kim, T. G. Lee, S. H. Cho, K. T. Lee, T. H. Lee, Y. W. Hong, C. H. Hong, J. S. Kim and S. Nahm, *Journal of the American Ceramic Society*, 2018, **101**, 3997-4010.

10. X. Lv, J. Wu, J. Zhu, D. Xiao and X. Zhang, *Journal of the European Ceramic Society*, 2018, **38**, 85-94.

11. T.-G. Lee, S.-H. Cho, D.-H. Kim, H.-G. Hwang, K.-T. Lee, C.-H. Hong, Y.-W. Hong, K. H. Chae, J.-W. Choi and J.-S. Kim, *Journal of the European Ceramic Society*, 2019, **39**, 973-985.

12. H. Kim, D.-S. Kim, S.-J. Chae, S.-H. Go, S.-W. Kim, D.-G. Lee, H.-C. Song, E.-J. Kim, J.-M. Eum and S. Nahm, *Ceramics International*, 2021.

13. K. T. Lee, T. G. Lee, S. W. Kim, S. J. Chae, E. J. Kim, J. S. Kim, J. W. Choi and S. Nahm, *Journal of the American Ceramic Society*, 2019, **102**, 6115-6125.

14. K.-T. Lee, D.-H. Kim, S.-H. Cho, J.-S. Kim, J. Ryu, C.-W. Ahn, T.-H. Lee, G.-H. Kim and S. Nahm, *Journal of Alloys and Compounds*, 2019, **784**, 1334-1343.

15. B. He, Y. Du, Y. Liu, J. Wang, W. Liu and H. Xu, *Journal of Materials Science: Materials in Electronics*, 2021, 1-11.

16. K. T. Lee, D. H. Kim, J. S. Park, T. G. Lee, S. H. Cho, S. J. Park, J. Y. Kang and S. Nahm, *Journal of the American Ceramic Society*, 2017, **100**, 4827-4835.

17. P. Jia, Y. Li, Z. Zheng, Z. Li, L. Cao and Y. Wang, *Journal of Alloys and Compounds*, 2021, 161799.

18. M. Jiang, J. Zhang, G. Rao, D. Li, C. A. Randall, T. Li, B. Peng, L. Li, Z. Gu and X. Liu, *Journal of Materials Chemistry C*, 2019, **7**, 14845-14854.

19. H. Liu, P. Veber, J. Rödel, D. Rytz, P. B. Fabritchnyi, M. I. Afanasov, E. A. Patterson, T. Frömling, M. Maglione and J. Koruza, *Acta Materialia*, 2018, **148**, 499-507.

20. J. Yang, F. Zhang, Q. Yang, Z. Liu, Y. Li, Y. Liu and Q. Zhang, *Applied Physics Letters*, 2016, **108**, 182904.

21. X. Huo, R. Zhang, L. Zheng, S. Zhang, R. Wang, J. Wang, S. Sang, B. Yang and W. Cao, *Journal of the American Ceramic Society*, 2015, **98**, 1829-1835.

22. J. Song, C. Hao, Y. Yan, J. Zhang, L. Li and M. Jiang, *Materials Letters*, 2017, **204**, 19-22.

23. H. Tian, X. Meng, C. Hu, P. Tan, X. Cao, G. Shi, Z. Zhou and R. Zhang, *Scientific reports*, 2016, **6**, 1-8.

24. H. Zhou, H. Deng, X. Liu, H. Yan, X. Zhao, H. Luo and J. Xu, *Ceramics International*, 2016, **42**, 15327-15331.

25. X. Huo, L. Zheng, S. Zhang, R. Zhang, G. Liu, R. Wang, B. Yang, W. Cao and T. R. Shrout, *physica status solidi (RRL)–Rapid Research Letters*, 2014, **8**, 86-90.

26. H. Deng, X. Zhao, H. Zhang, C. Chen, X. Li, D. Lin, B. Ren, J. Jiao and H. Luo, *CrystEngComm*, 2014, **16**, 2760-2765.

27. P. Li, J. Zhai, B. Shen, S. Zhang, X. Li, F. Zhu and X. Zhang, *Advanced materials*, 2018, **30**, 1705171.

28. D.-S. Kim, J.-M. Eum, S.-H. Go, H.-S. Shin, H. Kim, S.-J. Chae, S.-W. Kim, E.-J. Kim, J.-U. Woo and S. Nahm, *Journal of Alloys and Compounds*, 2021, 160662.

29. B. Liu, P. Li, B. Shen, J. Zhai, Y. Zhang, F. Li and X. Liu, *Journal of the American Ceramic Society*, 2018, **101**, 265-273.

30. B. Liu, P. Li, B. Shen, J. Zhai, Y. Zhang, F. Li and X. Liu, *Ceramics International*, 2017, **43**, 8004-8009.